Nanoscale

PAPER

View Article Online
View Journal

Cite this: DOI: 10.1039/c8nr01725e

High-throughput optical thickness and size characterization of 2D materials†

William W. Dickinson,[a] Harish V. Kumar,[b] Douglas H. Adamson[b] and Hannes C. Schniepp *[a]

Received 1st March 2018,
Accepted 10th April 2018

DOI: 10.1039/c8nr01725e

rsc.li/nanoscale

We describe a method using simple optical microscopy and image processing that simultaneously characterizes thousands of nanosheets in a sample area on the order of 1 mm^2. Including data acquisition and processing, both the number of atomic layers and the lateral sizes of all sheets can be obtained within a few hours—approximately 100 times faster than with previous methods, such as atomic force microscopy. This is achieved by normalizing the optical image based on substrate brightness, which eliminates inhomogeneities usually limiting optical techniques. Ultimately, the method enables robust statistical analysis of populations of nanosheet materials. We demonstrate the utility of this method by examining fractions made from a sample of graphene oxide (GO) made using an emulsion-based method. Beyond providing the morphological composition of the samples, the reported method is sensitive enough to provide information about the oxidation level of a population of GO sheets and, correspondingly, optical constants of the material.

Introduction

Nanosheet (2D) materials, such as graphene and graphene oxide (GO), exhibit several exceptional properties, including high strength and electrical conductivity,[1–3] with sheets having lateral dimensions greater than 10 μm exhibiting enhanced properties.[4–9] In many applications, single and few layer materials are also desired, because high surface area and high aspect ratios can be critical for composite and film performance. Despite the dual and concurrent importance of the relatively large lateral dimensions (tens of micrometres and above) and small thicknesses (typically a small number of atomic layers) of these materials, few methods exist for their simultaneous characterization. Currently, the most common and accurate method, atomic force microscopy (AFM), is lengthy and tedious. With many applications requiring knowledge of sheet size and thickness, there is a pressing need for more convenient and high-throughput methods to determine the lateral size of these nanomaterials. Here we introduce and apply an optical technique to simultaneously and conveniently obtain such data, and demonstrate its accuracy with extensive corroboration by more traditional AFM and X-ray diffraction (XRD) techniques.

Currently used methods for characterizing two-dimensional materials all face serious challenges in simultaneously and rapidly determining both the thickness and lateral size of statistically relevant sheet populations. Fluorescence microscopy has been used to enhance the contrast between nanosheets and a substrate, making it possible to examine many sheets at once using a low magnification image,[10,11] but it lacks information on the thickness of the sheets. Similarly, SEM can be used to image many sheets using a large viewing area, but determining the number of layers in a particular flake is challenging. In contrast, AFM can provide accurate measurements of sheet thickness and lateral dimensions,[12] but is comparatively slow. AFM images are typically limited to sizes of 100 μm by 100 μm, which limits the number of sheets per AFM image, requiring many images for statistically significant results. Raman spectroscopy is also used to examine 2D materials; however, the peaks for double- and few-layer graphene are difficult to distinguish,[13] especially in cases where surface functionalization causes additional peak shifts.[14] The technique probes a relatively small sample area while providing no information about lateral dimensions. In addition, fluorescence microscopy, SEM, AFM, and Raman all require specialized equipment and are expensive, both in capital and operating costs.

Our approach to the characterization of 2D nanomaterials is based on optical microscopy, which is affordable, fast, and covers large areas in a single image. Previous research has

[a]Department of Applied Science, The College of William & Mary, Williamsburg, VA 23185, USA. E-mail: schniepp@wm.edu
[b]Department of Chemistry and Institute of Materials Science Polymer Program, University of Connecticut, Storrs, CT 06269, USA

†Electronic supplementary information (ESI) available. See DOI: 10.1039/c8nr01725e

shown that optical microscopy is capable of visualizing different nanosheet materials, including graphene,[13,15] GO,[10,16] hexagonal boron nitride,[17] and numerous transition metal dichalcogenides (*e.g.* MoS_2, GaS, GaSe, WSe_2, and TaS_2).[13,18–20] By depositing the material on silicon substrates with a silicon dioxide layer of well-defined thickness, the number of layers can be determined based on intensity and colour variations of the reflected light, showing differences of a few percent, given appropriate choice of substrate and wavelength, at the level of individual flakes.[13,21] We have developed image processing techniques that eliminate the significant image inhomogeneities that are usually caused in such experiments by uneven illumination from standard light sources and optical aberrations, which can be an order of magnitude higher than the differences between layers. This enabled us to establish a calibration to determine sheet thickness from colour/brightness invariable within an image and across many images taken under the same conditions. Thus, we provide the first demonstration of a high-throughput technique to characterize thickness and size of thousands of nanosheets within a sample area on the order of 1 mm^2 within a few hours. Analysing the same area on a standard AFM would require about 100 scans, with manual sample translations after each scan. According to our estimates, this would take at least 100 times longer assuming ideal conditions.

Results and discussion

Optical image processing

Our optical imaging and image analysis procedure consisted of four major steps: (1) imaging, (2) removal of inhomogeneities, (3) conversion of brightness to sheet thickness, and (4) recognition of individual sheets. For imaging (1) of a substrate carrying the GO sheets of interest, we used a 20× objective, which was a good compromise between spatial resolution and the number of sheets imaged at a time. We set the lamp and camera exposure time to a high level for enhanced contrast; we found that the red colour channel exhibited the highest contrast as a function of the number of layers. To reduce sensor noise produced by our low-budget camera, 100 red channel images taken at the same location were averaged to produce a single 32-bit greyscale image (Fig. 1A). A false coloured version of the image (Fig. 1B) highlights the significant variation between the centre and edges. The correspondence between brightness and colour is given in the histogram in Fig. 1C. The broad peak in

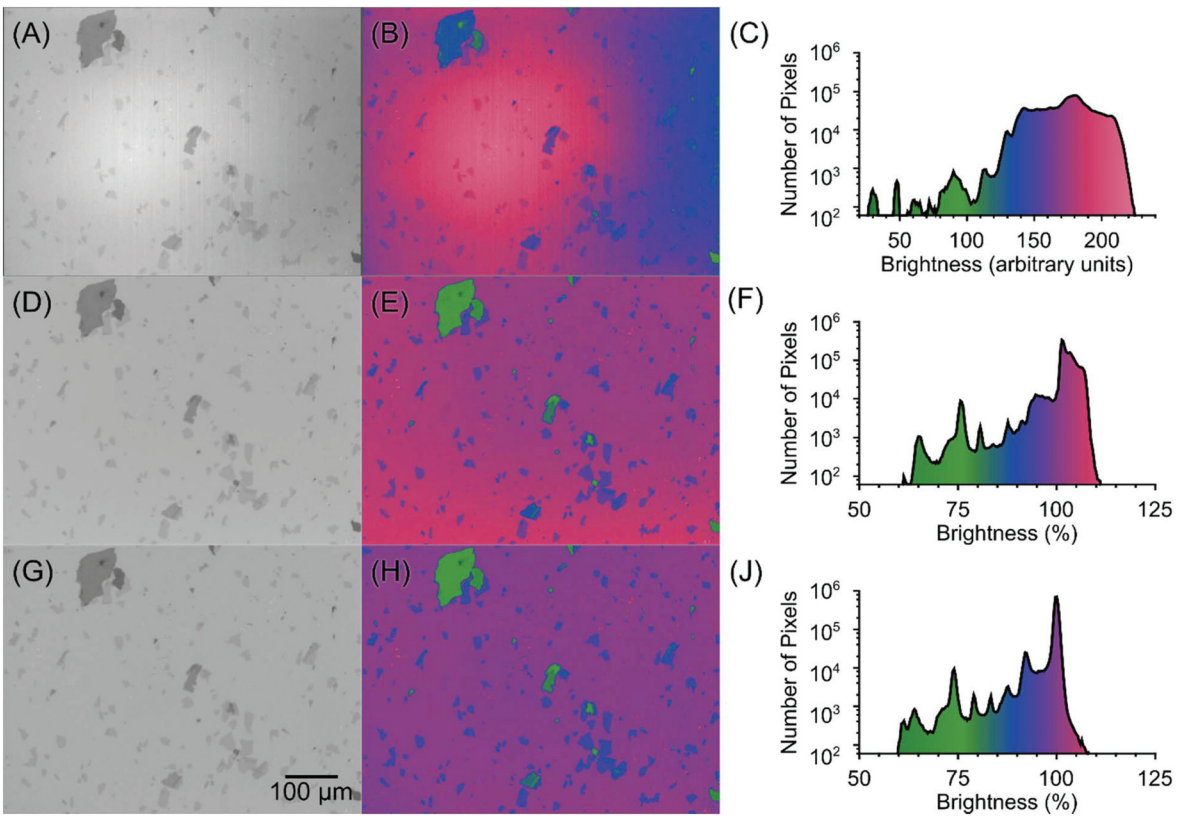

Fig. 1 Steps of the optical processing method applied to a sample of GO sheets on a Si substrate. (A) Average of the red channel of 100 images. (B) False coloured version of (A) demonstrating the brightness variations across the image. (C) Corresponding brightness histogram of (A, B). (D) Image after division by the empty substrate image (with corresponding false colour image (E) and histogram (F)). (G) Image after flattening in Gwyddion (with corresponding false colour image (H) and histogram (J)). The pixel intensities on the *x*-axis in (C) reflect those from the original camera, whereas those in (F) and (J) were normalized for the substrate peak to be at 100.

this histogram, spanning from blue to red, is large relative to the contrast between the sheets and illustrates the inhomogeneities in brightness due to the optical imaging system and the illumination. To reduce these inhomogeneities, a background was established by acquiring 100 images of a bare substrate using the same imaging system and averaging the red channels into another 32-bit greyscale image (not shown). Fig. 1D shows the results of dividing Fig. 1A by this background using ImageJ.[22] The false coloured version of this image (Fig. 1E) shows the improved consistency of brightness across the image. The highest peak in the corresponding brightness histogram (Fig. 1F) represents the substrate; however, this peak still spans from purple to red, and individual layer numbers of flakes are not yet consistently discernible as peaks in the histogram.

Further enhancement of the images was obtained by utilizing Gwyddion,[23] a software package normally used to process scanning probe microscopy images. In particular, we used the "remove polynomial background" routine, where we first selected pixels with the brightness representing the substrate *via* thresholding and then performed a planar fit on this subset of pixels. The polynomial order of planar fit required depends on the optical system used; the most appropriate order can be determined by comparing the histograms from images processed with different order planar fits. For our system, the peaks in the histogram significantly narrowed up to second order fits, with very little further improvements for higher orders, as illustrated in Fig. 2. We found that carrying out fits at higher orders than necessary comes at the risk of introducing artifacts and thus reducing accuracy. We then divided Fig. 1D by this fitted plane. The results are shown in Fig. 1G. The false coloured version of this image (Fig. 1H) shows that this significantly increases the homogeneity of the brightness across the image, which now has a consistent purple colour for all portions of the substrate. Additionally, the corresponding histogram (Fig. 1J) now shows more discernible peaks associated with individual layer numbers, along with a narrowed peak for the substrate, as compared to (Fig. 1F).

As a next step, we determined the brightness levels corresponding to the substrate and each layer number. In principle, this can be accomplished in different ways, depending on the material, the specific sample and the desired accuracy. For some materials, an equation relating brightness and number of layers is available from the literature (*e.g.* graphene[24]) and can be used as given. In the case of graphene oxide, such an equation is not available; however, by performing AFM scans co-located with our optical images, shown in Fig. 3, we were able to correlate layer numbers with peaks in the optical brightness histogram (Fig. 4A). A linear fit was sufficient for samples where a small range of layer numbers were present (Fig. 4B). The brightness difference between the substrate and the material is often different from that separating different layers of the material itself, and so was not included in our fit. Once this curve was established for the material, further AFM scans were not needed to process other images.

It is worth noting that the curve relating brightness to layer number becomes noticeably non-linear outside particular ranges of layer numbers, and can even be non-monotonic, *i.e.* at certain peak intensities contrast inversion can be observed.[13,21] An example of this is shown in Fig. 5A, where the majority of the flake is dark compared to the substrate. However, in the centre of the flake, the brightness increases and even exceeds substrate brightness. In the simple thresholding procedure described above, this bright area would not be recognized as a part of the flake, although in fact it is a particularly thick area of the flake. To account for this, we developed an image processing algorithm to extend our model to include this kind of contrast inversion, making higher numbers of layers accessible and significantly increasing the accuracy of the average layer number observed in a particular sheet.

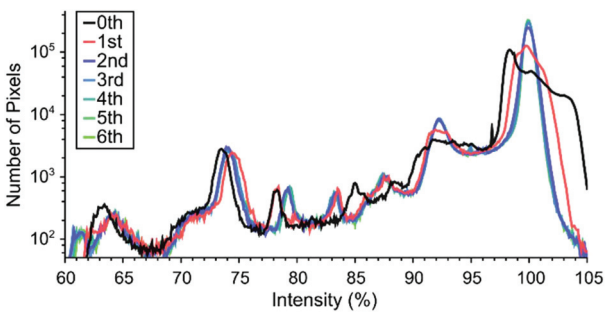

Fig. 2 Histograms of images obtained by dividing Fig. 1D by different order planar fits from Gwyddion. The second order fit (blue), essentially the histogram shown in Fig. 1J, is a clear improvement over zero (black) and first (red) order fits. Higher orders offer no significant advantages.

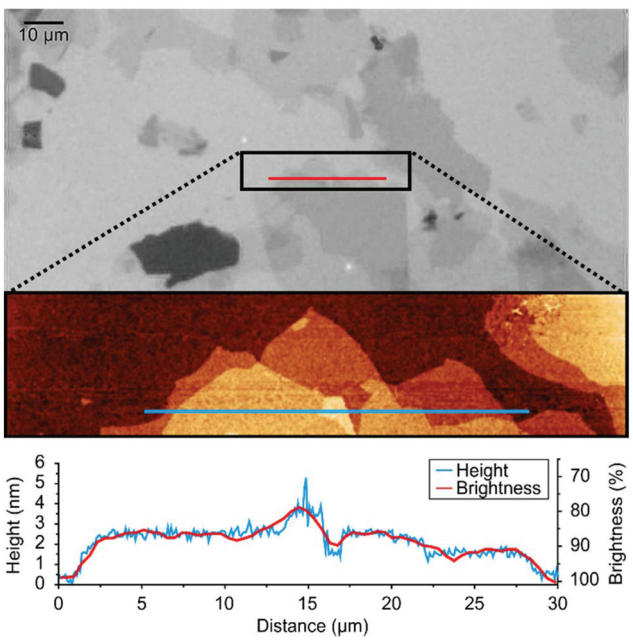

Fig. 3 Co-located optical image (top) and AFM scan (centre) of GO sheets on silicon substrate. The position of the 30 μm long profile is indicated in both images. Corresponding AFM height profile (blue line, left axis) and optical brightness profile (red line, right axis) are shown in the bottom panel.

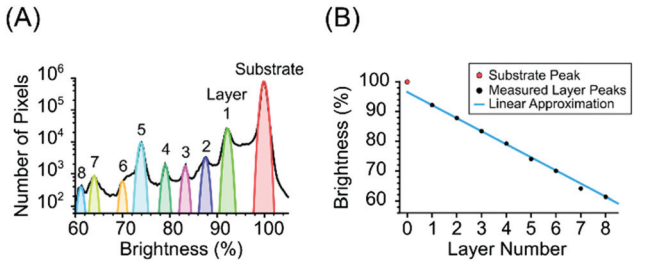

Fig. 4 The histogram from Fig. 1F with the peaks corresponding to the substrate and various layers identified (A) and a plot (B) of the measured substrate (red circle) and layer peak positions (black circles) and a linear approximation made using only the spacing between the single and double layer peaks (blue line).

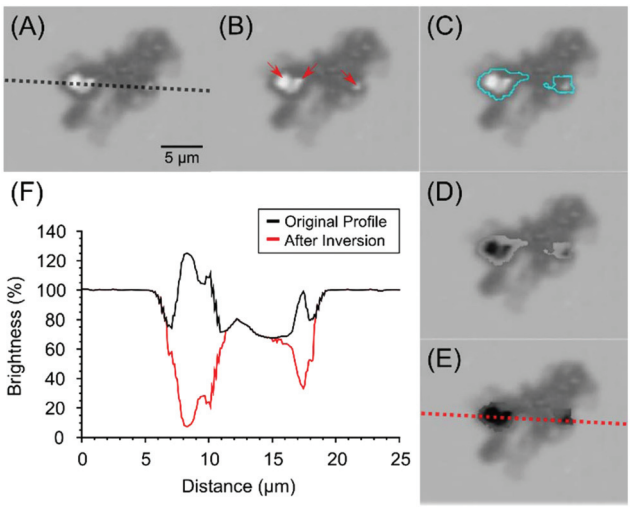

Fig. 5 Steps of the inversion process with a GO flake on a Si substrate: (A) original flake, (B) locations of local maxima (red points), (C) boundary of regions to be inverted (blue), (D) flake after initial brightness inversion, (E) after matching boundary intensities. (F) Optical brightness profiles before (black) and after (red) inversion.

To correct for contrast inversion we wrote an ImageJ macro selectively inverting these regions (see ESI†), with the goal of making the image brightness monotonic as a function of sheet thickness. The macro first identifies local maxima within the flake (Fig. 5B) and recursively examines adjacent pixels. As long as brightness values are falling, pixels are added to an area surrounding each maximum (Fig. 5C). This procedure establishes a boundary line around each maximum, marking the onset of the brightness inversion. Finally, the brightness values within each boundary are inverted (Fig. 5D) and an offset applied to avoid a discontinuity at the boundary (Fig. 5E). The final effect of this process can be seen in the brightness profiles in Fig. 5F, with the original profile in black and the inversion processed profile in red. After completing this inversion, we were able to convert the image brightness directly into a number of layers for the entire image (Fig. 4B), which was accomplished using the "Process > Math > Macro..." command in ImageJ.

The final step after optimizing the acquired images and converting them into thickness maps (steps 1–3), was to generate the sheet size and thickness distributions. We first identified areas belonging to a sheet using a thickness threshold of 0.5 layers. Next, the particle analysis routine built into ImageJ was used to generate a list of sheets, including the area and average layer number for each sheet. The sheet area is a well-defined measure, and we have thus used it to represent each sheet's lateral size; other choices for metrics characterizing sheet sizes can be used. This information was analysed to examine population distributions.

GO sample analysis

In order to demonstrate the capability and potential of the described optical technique, it was tested on a batch of material in which we separated a single GO sample into 2 fractions and characterized each fraction. These fractions—labelled as GOe and GOw—were made using a recently described fractionation method based on a chloroform-in-water emulsion,[25] effectively an oil-in-water emulsion due to the non-polar nature of chloroform. The result is two fractions: an upper aqueous fraction with suspended GO and a lower fraction of hydrophobic chloroform droplets stabilized by a thin skin of GO. Separation of these two layers provides what is termed GOw, for the water fraction, and GOe, for the emulsion fraction. In the original study, analysis by XRD, Raman spectroscopy, and elemental analysis showed that the water fractions contain a higher degree of oxidation than do the emulsion fractions.[25] Information as to the lateral dimensions of the fractions or the number of layers in the resulting GO fraction, however, was not determined in the published study. This fractionation system thus provides an opportunity to demonstrate the utility of our optical image analysis approach.

Both fractions, as well as the original, unfractionated GO, were analysed using our optical technique. Three locations were imaged for each sample, which required only a few hours to process, but provided information on hundreds of flakes for each sample (over 2000 in the GO sample alone). An example of these images for each sample is provided in the ESI.† The results were plotted as a function of both sheet thickness and lateral sheet size, as shown in Fig. 6A/B and C/D, revealing that the fractionation method is not only selective with respect to the degree of oxidation,[25] but also with respect to sheet size and thickness. Fig. 6A shows the cumulative surface area fraction as a function of average layer number. Here, nearly 90% of the surface area of the GOe sample was from sheets with an average layer number of one, while no sheet had an average layer number of more than 4. In contrast, only 10% of the surface area in GOw was from sheets that were 4 layers thick or less. This four layer mark also showed a transition in the original GO sample: it matched the GOw sample closely after this mark, but showed a comparatively higher percentage of low layer material before it. Fig. 6B shows the distributions by total number of sheets at each thickness. This showed the close alignment in the distributions of sheets in both the GO and GOw samples at layer numbers greater than four. It also

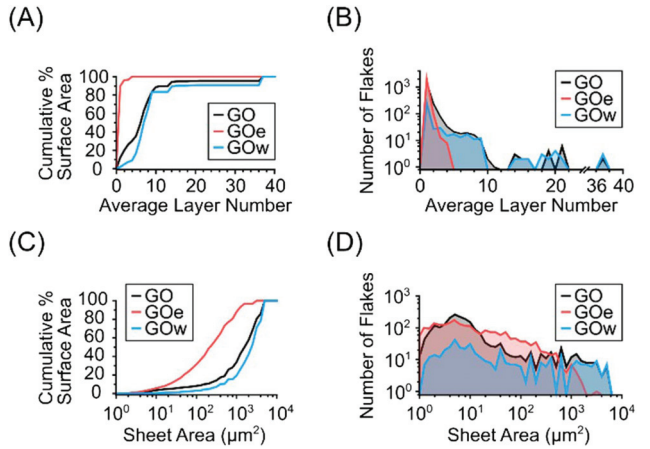

Fig. 6 Cumulative percentage of total sheet surface area (A) and number of sheets characterized (B) as a function of average layer number. Cumulative percentage of total sheet surface area (C) and number of sheets characterized (D) as a function of sheet area.

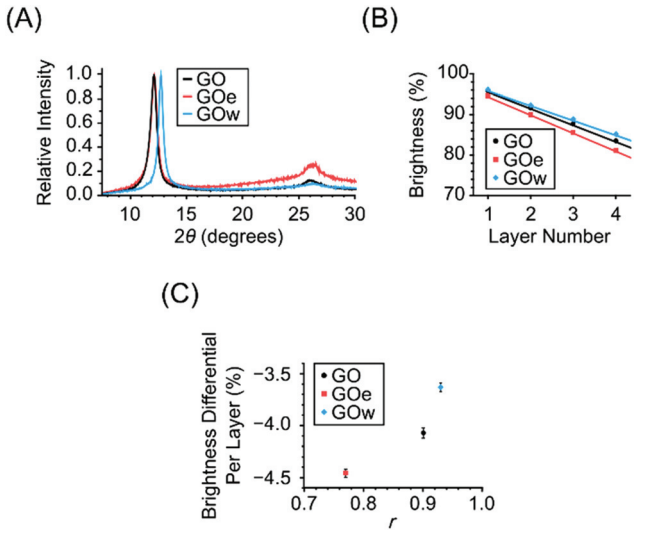

Fig. 7 (A) XRD spectra of fractionated GO samples. (B) Brightness values for the first 4 layers for each of the samples, with linear fits. (C) Brightness differential per layer (slope of the linear fits from (B)) plotted against the corresponding *r* value.

demonstrated the large impact of higher layer number flakes, which contain a large portion of total surface area despite their small numbers. For ensemble analysis as a function of sheet size we prepared the histograms shown in Fig. 6C and D, where a log scale was used on the horizontal axis. Ten bins of equal width on a log scale were used per decade. Fig. 6C shows the cumulative area fraction by sheet size: over 80% of the total surface area in the GOe fraction came from sheets with areas of less than 1000 μm^2. This is compared to approximately 25% in the original GO sample, and only 15% in the GOw sample. Fig. 6D shows the distribution of total number of sheets by sheet area. All samples showed more smaller sheets than larger ones, and all had a decreasing number of sheets as the size increased. All sheets in the GOe sample were less than 2000 μm^2, but the sizes of the GO and GOw samples extend out to almost 6000 μm^2.

As shown in Fig. 6A and C, the fractionation method was selective to both sheet size and layer number. The sheets in the emulsion portion (GOe) were systematically smaller and thinner compared to the original GO solution; accordingly, the water portion (GOw) systematically retained sheets that were larger and had higher layer numbers. This was most apparent in the layer number distributions of the GO and GOw samples before and after the 4 layer mark and in the convergence of size distributions of GO and GOw after the initial separation in the smaller sheet regime. Interestingly, both samples featured correlated spikes in their layer number distributions at 12–14, 18–21, and 37 layers. Similarly, the sheet area of both samples exhibited pronounced peaks, for instance at 180, 400, and 600 μm^2. The fact that both GO and GOw independently showed these peaks, while they are absent in the GOe sample, suggests that these sizes and thicknesses were already over-represented in the original graphite.

For further insight, the samples were also analysed using XRD. As typical for samples produced by oxidizing graphite, XRD spectra of the GO fractions showed two peaks (Fig. 7A). The peak around $2\theta = 26°$ corresponds to a separation of about 0.34 nm, representing the original stacking of graphitic sheets prior to oxidation. The peak at $2\theta = 10°$–$13.5°$ represents the increase in spacing between the sheets to 0.7–0.9 nm caused by the addition of oxygen functional groups during the reaction. To quantify to what degree the material exhibited the increased spacing due to oxidation, we calculated an XRD *r* value based on the formula[25] $r = A_{GO}/(A_{GO} + A_G)$, where A_G is the area of the G peak assigned to graphite stacking, and A_{GO} the area of the GO peak assigned to GO stacking. Table 1 lists the XRD *r* values for each of the three samples. There is a clear order in the *r* value, with GOw > GO > GOe, which is in line with published results using this fractionation method.[25] This ordering is similar to that found for sheet size and average layer thickness using the optical method, with a larger portion of oxidized material corresponding to a greater percentage of large or many layer sheets. This correlation illuminated the underlying mechanism of the fractionation process. The GOe fraction has undergone a significant degree of exfoliation as compared to the GOw fraction. In hindsight this is not surprising, as the emulsion is stabilized by the spreading (exfoliation) of sheets at the oil/water interface.[26] This means that not only are the less oxidized (less hydrophilic) sheets found at the oil/water interface, but they are exfoliated at the interface as well.

Table 1 Comparison of graphitic content for each sample using an XRD based *r* value. Higher values indicate a higher percentage of graphite oxide content compared to graphite. Error values are standard deviation

Sample name	XRD *r* value
GOw	0.932 ± 0.005
GO	0.898 ± 0.004
GOe	0.768 ± 0.016

Thus the degree of oxidation, as determined by the value of r, only partially describes the state of the GO. This additional information would have remained unobserved without the rapid morphological characterization made possible by the optical method outlined here.

It is interesting to compare this correlation between larger sheet dimensions and higher oxidation levels with the work of Dimiev and Tour, who showed that the oxidation of graphite into graphite oxide during the Hummers method is controlled by the diffusion rate of the oxidizing agent.[27] This could possibly lead one to expect that larger sheets would be less oxidized than smaller ones. At first glance, our results appear to contradict this expectation, although we do not believe this is the case. Rather, the more hydrophobic, nearly un-oxidized graphite in the GO sample went to the oil/water interface, which has been shown to drive exfoliation.[25] The more hydrophilic, highly oxidized material, in contrast, remained in the aqueous phase and thus did not exfoliate and so remained larger and more stacked on average. This was seen in the difference in the distribution of sheets with an average layer number less than four in Fig. 6A.

It has been shown that oxidation of graphene changes its optical properties,[16,28,29] consequently, we were interested whether different degrees of oxidation found in the different kinds of material (GOw, GO, GOe) would lead to a noticeable difference in the brightness-*vs*.-thickness curves for different materials. Therefore, a linear fit was applied to the brightness values for the first four layers for each sample (Fig. 7B). The brightness change per layer was determined from the slope of this fit for each material and showed a surprisingly strong and significant change as a function of the r value (Fig. 7C). The difference in slope between the three materials was large compared to the corresponding error of the fit (shown as error bar). The slope of GO, $(-4.08 \pm 0.04)\%$, was significantly greater compared to GOe, $(-4.46 \pm 0.03)\%$, and significantly less than GOw, $(-3.63 \pm 0.04)\%$. As the change in brightness for a given nanosheet layer number is dependent on the dielectric constant of the material,[21] our simple method provides surprisingly powerful way to assess optical properties of a population; in principle, one could calculate the optical constants of the material using this method.

Conclusions

In conclusion, the technique described here stems from a unique combination of low-magnification optical microscopy, image processing techniques developed for AFM analysis, and the use of commercially available substrates for imaging 2D materials. Our technique is quick, straightforward, low-cost, works for a variety of materials, and is robust over large areas, thus providing global characterization of an ensemble of nanosheets. The method also offers a simple means of assessing the oxidation state and optical constants of a material without additional processing. The utility of this approach was demonstrated by characterizing a set of GO samples fractionated based on the degree of oxidation through the use of a water/chloroform emulsion. Our results clearly revealed the distinct morphological differences among the different fractions, illuminating the differences in the sample compositions. We expect the dramatic reduction in characterization time of our approach will be useful in both the commercial development and academic studies of nanosheet materials.

Experimental methods

Graphite oxide synthesis

Graphite oxide was synthesized using the Hummers method.[30] First, 25 mL of sulphuric acid (Fisher Scientific, ACS Plus) and 500 mg of sodium nitrate (Acros Organics, 99% +) were added to a 4 L round bottom flask. The mixture was stirred until dissolved. Then, 1 g graphite (Ashbury Mills, natural flake Grade 3243) was added to the flask and stirred until evenly dispersed. Next, 3 g of potassium permanganate (EM Sciences, GR ACS) was added to the reaction mixture. The potassium permanganate was added slowly (over 10 min) to keep the temperature low. After 90 minutes, 250 mL of DI water and 20 mL of hydrogen peroxide (Acros Organics, 35 wt%) were added to the reaction vessel to quench the reaction. Then, 25 mL of concentrated hydrochloric acid (Sigma Aldrich, 37%) was added to solubilize the salts in the reaction container. Further steps involved purification of the obtained product using filtration and multiple centrifugations.

Fractionation of graphite oxide

To fractionate the GO, 40 mg of GO, 10 mL of deionized water, and 10 mL of chloroform (Fisher, ACS grade, used without further purification) was mixed for one minute using a Kinematica Brinkmann Polytron Homogenizer mixer (Model PT 10-35) to obtain an oil-in-water emulsion. The water phase (containing GOw) and emulsion phase (containing GOe) were removed from the fractionation vial separately.

Sample preparation for optical imaging

To prepare the samples for optical imaging, they were dried under vacuum at room temperature for more than two weeks. They were then suspended in water by one hour stirring with a magnetic spin bar followed by two minutes of mild sonication by bath sonication, then an additional several hours of stirring. The samples were spin-coated (Laurell WS-400Bz-6NPP-Lite Spin Processor) for 3 minutes at 3000 rpm onto silicon substrates with a 300 nm SiO_2 layer (Graphene Supermarket). The substrates had previously been cleaned by sonication (Fisher Scientific FS30D bath sonicator) in ultrapure water (Synergy UV water purification system, EMD Millipore) with surfactant (Contrad 70, Decon Labs) for 30 minutes at 60 °C followed by 30 minutes under UV/ozone (Novascan PSDP-UV_4TUV).

Optical and AFM imaging

Optical images were taken using an Olympus inverted microscope (Model: IX71) with two objectives (MPLFLN-BD 20× (0.45 NA)) and (LUCPLFLN, 40× (0.6 NA)), equipped with an EXFO X-Cite Series 120 lamp and a Big Catch EM-C320C camera. Images were captured with ScopePhoto software and then processed with ImageJ (http://imagej.net/) and Gwyddion (http://gwyddion.net/). AFM data was captured using an NTEGRA Prima (NT-MDT) used in dynamic mode under ambient conditions. Silicon probes (HQ:NSC15/AL BS, Mikromasch) with a nominal spring constant of 40 N m^{-1} and a resonant frequency of 325 kHz were used for these scans.

XRD analysis method

XRD analysis was performed using a 2D X-ray diffractometer (Bruker D2 Phaser) with radiation of wavelength 1.54 Å. The sample was prepared by drop casting GO water suspension onto a glass slide, followed by drying at 70 °C overnight prior to measurement. GO and G peak areas were calculated using the Bruker D2 Phaser instrument software. The net peak area was calculated in the 2θ range of 10° to 14° for the A_{GO} peak and 24° to 28.5° for the A_G peak. Tests were performed for three samples from each fraction. Values reported are the means of these tests with standard deviations given as error.

Conflicts of interest

There are no conflicts to declare.

Acknowledgements

This material is based upon work supported by the National Science Foundation under Grant No. DMR-1352542, DMREF-1534428, and DMREF-1535412.

References

1 S. Z. Butler, S. M. Hollen, L. Cao, Y. Cui, J. A. Gupta, H. R. Gutiérrez, T. F. Heinz, S. S. Hong, J. Huang, A. F. Ismach, E. Johnston-Halperin, M. Kuno, V. V. Plashnitsa, R. D. Robinson, R. S. Ruoff, S. Salahuddin, J. Shan, L. Shi, M. G. Spencer, M. Terrones, W. Windl and J. E. Goldberger, *ACS Nano*, 2013, **7**, 2898–2926.
2 R. Sengupta, M. Bhattacharya, S. Bandyopadhyay and A. K. Bhowmick, *Prog. Polym. Sci.*, 2011, **36**, 638–670.
3 R. J. Young, I. A. Kinloch, L. Gong and K. S. Novoselov, *Compos. Sci. Technol.*, 2012, **72**, 1459–1476.
4 G. Eda and M. Chhowalla, *Adv. Mater.*, 2010, **22**, 2392–2415.
5 G. Eda, Y.-Y. Lin, C. Mattevi, H. Yamaguchi, H.-A. Chen, I.-S. Chen, C.-W. Chen and M. Chhowalla, *Adv. Mater.*, 2010, **22**, 505–509.
6 Z. Luo, Y. Lu, L. A. Somers and A. T. C. Johnson, *J. Am. Chem. Soc.*, 2009, **131**, 898–899.
7 C.-Y. Su, Y. Xu, W. Zhang, J. Zhao, X. Tang, C.-H. Tsai and L.-J. Li, *Chem. Mater.*, 2009, **21**, 5674–5680.
8 N. R. Wilson, P. A. Pandey, R. Beanland, R. J. Young, I. A. Kinloch, L. Gong, Z. Liu, K. Suenaga, J. P. Rourke, S. J. York and J. Sloan, *ACS Nano*, 2009, **3**, 2547–2556.
9 J. Zhao, S. Pei, W. Ren, L. Gao and H.-M. Cheng, *ACS Nano*, 2010, **4**, 5245–5252.
10 E. Treossi, M. Melucci, A. Liscio, M. Gazzano, P. Samori and V. Palermo, *J. Am. Chem. Soc.*, 2009, **131**, 15576–15577.
11 A. Liscio, K. Kouroupis-Agalou, X. D. Betriu, A. Kovtun, E. Treossi, N. M. Pugno, G. D. Luca, L. Giorgini and V. Palermo, *2D Mater.*, 2017, **4**, 025017.
12 G. Gonçalves, M. Vila, I. Bdikin, A. de Andrés, N. Emami, R. A. S. Ferreira, L. D. Carlos, J. Grácio and P. A. A. P. Marques, *Sci. Rep.*, 2014, **4**, 6735.
13 H. Li, J. Wu, X. Huang, G. Lu, J. Yang, X. Lu, Q. Xiong and H. Zhang, *ACS Nano*, 2013, **7**, 10344–10353.
14 K. N. Kudin, B. Ozbas, H. C. Schniepp, R. K. Prud'homme, I. A. Aksay and R. Car, *Nano Lett.*, 2008, **8**, 36–41.
15 P. Blake, E. Hill, A. C. Neto, K. Novoselov, D. Jiang, R. Yang, T. Booth and A. Geim, *Appl. Phys. Lett.*, 2007, **91**, 063124.
16 F. Perrozzi, S. Prezioso, M. Donarelli, F. Bisti, P. D. Marco, S. Santucci, M. Nardone, E. Treossi, V. Palermo and L. Ottaviano, *J. Phys. Chem. C*, 2012, **117**, 620–625.
17 R. V. Gorbachev, I. Riaz, R. R. Nair, R. Jalil, L. Britnell, B. D. Belle, E. W. Hill, K. S. Novoselov, K. Watanabe, T. Taniguchi, A. K. Geim and P. Blake, *Small*, 2011, **7**, 465–468.
18 D. J. Late, B. Liu, H. Matte, C. Rao and V. P. Dravid, *Adv. Funct. Mater.*, 2012, **22**, 1894–1905.
19 H. Li, G. Lu, Z. Yin, Q. He, H. Li, Q. Zhang and H. Zhang, *Small*, 2012, **8**, 682–686.
20 K. S. Novoselov, D. Jiang, F. Schedin, T. J. Booth, V. V. Khotkevich, S. V. Morozov and A. K. Geim, *Proc. Natl. Acad. Sci. U. S. A.*, 2005, **102**, 10451–10453.
21 S. Roddaro, P. Pingue, V. Piazza, V. Pellegrini and F. Beltram, *Nano Lett.*, 2007, **7**, 2707–2710.
22 C. A. Schneider, W. S. Rasband and K. W. Eliceiri, *Nat. Methods*, 2012, **9**, 671–675.
23 D. Necas and P. Klapetek, *Open Phys.*, 2012, **10**, 181–188.
24 I. Jung, M. Pelton, R. Piner, D. A. Dikin, S. Stankovich, S. Watcharotone, M. Hausner and R. S. Ruoff, *Nano Lett.*, 2007, **7**, 3569–3575.
25 H. V. Kumar, S. J. Woltornist and D. H. Adamson, *Carbon*, 2016, **98**, 491–495.
26 S. J. Woltornist, A. J. Oyer, J.-M. Y. Carrillo, A. V. Dobrynin and D. H. Adamson, *ACS Nano*, 2013, **7**, 7062–7066.
27 A. M. Dimiev and J. M. Tour, *ACS Nano*, 2014, **8**, 3060–3068.
28 S. Kumar, M. Anija, N. Kamaraju, K. S. Vasu, K. S. Subrahmanyam, A. K. Sood and C. N. R. Rao, *Appl. Phys. Lett.*, 2009, **95**, 191911.
29 K. P. Loh, Q. Bao, G. Eda and M. Chhowalla, *Nat. Chem.*, 2010, **2**, 1015–1024.
30 W. S. Hummers and R. E. Offeman, *J. Am. Chem. Soc.*, 1958, **80**, 1339–1339.